Published in final edited form as:
Phys Med Biol. 2006 August 7; 51(15): 3785–3808.

Liver ablation guidance with acoustic radiation force impulse imaging:

Challenges and opportunities

B J Fahey[1], **S J Hsu**[1], **P D Wolf**[1], **R C Nelson**[2], and **G E Trahey**[1,2]

1*Department of Biomedical Engineering, Duke University, Durham, NC, USA*

2*Department of Radiology, Duke University Medical Center, Durham, NC, USA*

Abstract

Previous studies have established the feasibility of monitoring radiofrequency (RF) ablation procedures with acoustic radiation force impulse (ARFI) imaging. However, questions remained regarding the utility of the technique in clinically realistic scenarios and at scanning depths associated with abdominal imaging in adults. We address several of these issues and detail recent progress towards the clinical relevance of the ARFI technique. Results from *in vitro* bovine tissues and an *in vivo* ovine model are presented. Additional experiments were conducted with a tissue-mimicking phantom and parallel receive tracking techniques in order to further support the clinical feasibility of the method. Thermal lesions created during RF ablation are visualized with high contrast in both *in vitro* and *in vivo* hepatic tissues, and radial lesion growth can be monitored throughout the duration of the procedure. ARFI imaging is implemented on a diagnostic ultrasonic scanner, and thus may be a convenient option to guide RF ablation procedures, particularly when electrode insertion is also performed with sonographic guidance.

1. Introduction

Minimally invasive ablation procedures have become increasingly popular treatment options for malignancies located in tissue regions such as the liver, kidney, breast and prostate. Radiofrequency (RF) ablation is the most widely used ablation method for treating liver malignancies and is typically implemented when the patient is not a candidate for surgical resection or refuses surgery. RF ablation uses radiofrequency currents to induce localized ionic agitation, and thus frictional heating, in selected regions of tissue, with the end goal being the thermal destruction of the target malignancy (Dodd *et al* 2000). RF ablation offers several advantages, including feasibility for use in patients unsuitable for surgical resection due to either insufficient hepatic functional reserve or tumour location, reduced morbidity and mortality relative to surgical resection, and reduced treatment costs and hospital stay durations (Livraghi *et al* 2000, 2001).

Medical imaging has multiple roles in aiding RF ablation procedures. One such role is in guiding electrode placement during its transcutaneous insertion into the target tumour. Electrode placement is challenging yet generally successful when the tumour and electrode tip are ultrasonically visualized, especially when three-dimensional (3D) ultrasonic imaging is utilized (Xu *et al* 2003). For many patients, however, the target malignancy either is not ultrasonically visible or is inadequately visualized to guide electrode placement. These patients may be excluded from ablation treatments or, at some institutions, treated using computed

E-mail: brian.fahey@duke.edu.

tomography (CT) or magnetic resonance imaging (MRI) guidance of electrode placement. CT-fluoroscopic guidance is currently employed for these patients at Duke University Medical Center and other institutions (Dodd *et al* 2001, Choi *et al* 2003, Garcea *et al* 2003, Mayo-Smith *et al* 2003). The use of CT and CT-based fluoroscopic imaging for electrode placement markedly increases the time and complexity of the procedure. CT-guided procedures are undertaken with the patient positioned on the CT table and typically involve multiple and iterative CT/fluoroscopy exposures to guide electrode placement. Real-time electrode placement by CT/fluoroscopic guidance is rarely used, given the radiation exposures involved, particularly to the operator. CT-guided electrode placement often requires more than half an hour of placement time and involves some radiation exposure to the patient, radiologist and anaesthesiologist. MR guidance of liver ablation generally involves the use of an open-magnet MR system and MR-compatible ablation tools and is currently used at very few institutions (Oudkerk *et al* 2002, Kelekis *et al* 2003).

To be considered successful, an RF ablation procedure must induce coagulative necrosis throughout the entire tumour volume, plus a 0.5-1 cm rim of surrounding non-tumorous hepatic parenchyma (Dodd *et al* 2000). In addition, thermal lesion sizes must be controlled in order to avoid damaging nearby sensitive tissues, such as the diaphragm, gallbladder, bowel and major blood vessels, and to minimize damage to tissues beyond desired ablation margins. Currently, CT and/or MR are considered the 'gold standards' at many institutions for assessing the success of RF ablation procedures. However, in the early post-operative period, reactive hyperaemia at the edges of the thermal lesion may mimic residual tumour on CT or MR scans, and thus assessment imaging at many institutions is not scheduled until weeks following the initial RF ablation treatment. Recently, preliminary studies have suggested that positron emission tomography (PET) may be more sensitive than CT or MR methods for early (1 week) detection of residual tumour (Anderson *et al* 2003, Donckier *et al* 2003). However, none of these approaches provides the physician performing the procedure with vital information concerning induced lesion size while the patient is still on the operating table. As a recent study (Montgomery *et al* 2004) has demonstrated that identical ablation equipment and treatment protocols can produce lesions of markedly different sizes in different patients, monitoring the size of the induced thermal lesion during RF ablation procedures is essential to optimize the safety and success of the technique.

Many physicians currently rely solely on ultrasound images for real-time information and feedback during RF ablation procedures. However, ultrasonic imaging is notoriously insensitive to local variations in tissue temperature and is usually incapable of detecting ablation sites, even when the tissue has been desiccated and the protein denatured (Malcolm and Ter Haar 1996, Krouskop *et al* 1998, Gertner *et al* 1998, Righetti *et al* 1999). Thermal lesions that are visualized under ultrasound may be hyperechoic, hypoechoic or isoechoic (Cha *et al* 2000) and may be overestimated or underestimated in size (Lorentzen *et al* 1997). The creation of echogenic regions during RF ablation is a well-documented phenomenon and results from microbubble formation that occurs when tissue temperatures rise beyond the vaporization threshold, which was estimated by Kruskal *et al* (2001) to be 95 ° C at the electrode tip. The size of the induced microbubble cloud has been used by some physicians as a guide for initial estimates of lesion size, but has been demonstrated as unreliable as a means for demarcating necrotic tissue regions (Solbiati *et al* 1999, Raman *et al* 2000, Leyendecker *et al* 2002). In addition, the formation of bubbles is not always observed (Leyendecker *et al* 2002) and the size of the microbubble cloud has been shown to decrease significantly in as little as 2-5 min after ablation (Raman *et al* 2000). Factors such as blood perfusion and saline injection (i.e. wet electrodes) during RF ablation can drive bubbles away from the lesion site, further decreasing their utility in guiding ablations.

There have been several imaging methods proposed to increase the information available to physicians during RF ablation procedures. The use of contrast-enhanced ultrasound (CEUS) for detection of residual vasculature in intended ablation regions appears promising and is particularly beneficial since it can be performed as early as 10-15 min following the RF ablation procedure, while the patient is still under general anaesthesia (Solbiati *et al* 1999,2004,Choi *et al* 2003). However, this technique is still in its infancy and the required contrast agent is currently not approved for this application by the United States FDA. Elastography takes an alternate approach, differentiating the developing thermal lesion from untreated tissue based upon the differing mechanical properties of the two tissue regions (Varghese *et al* 2002,2003, 2004,Varghese and Shi 2004). Strain images can be created via a variety of compression techniques, and lesion size in strain images has been shown to correlate strongly with results from pathology (Liu *et al* 2004). However, each compressional technique is associated with disadvantages, such as limits on thermal lesion depth for feasible visualization and signal decorrelation due to out-of-plane tissue motion.

We propose the use of acoustic radiation force impulse (ARFI) imaging for assisting RF ablation procedures. ARFI imaging has previously been shown to be capable of visualizing *ex vivo* liver metastases (Fahey *et al* 2005b) and *in vivo* breast malignancies (Sharma *et al* 2004) with significant contrast, and we hypothesize that ARFI may obviate the need for CT/ fluoroscopy guidance of ablation electrode placement when the target tumour is not well visualized with ultrasound. Previous work has also demonstrated that ARFI imaging can accurately visualize RF ablation lesions induced in *ex vivo* hepatic and *in vivo* cardiac tissues (Fahey *et al* 2004, 2005a). ARFI imaging has several potential advantages for monitoring RF ablation procedures clinically. Radiation force methods are capable of imaging abdominal tissues at clinically realistic depths (8+ cm) (Fahey *et al* 2005b) without inducing large tissue strains in the near field. Additionally, ARFI imaging is implemented entirely on a diagnostic ultrasound scanner, and thus would not complicate or add cost to an RF ablation procedure. Further, real-time ARFI image visualization may provide the physician performing the procedure instantaneous feedback concerning the size of the developing thermal lesion.

In this paper, we investigate the utility of ARFI imaging for ablation monitoring in clinically realistic scenarios. Results are presented from studies of ARFI monitoring of RF ablation procedures in *in vitro* bovine and *in vivo* ovine hepatic tissues. In these experiments, induced thermal lesions were of relevant size and located at realistic depths for abdominal applications. Results from tissue-mimicking phantom studies and an experiment involving parallel receive tracking that are related to the clinical feasibility of the technique are also presented. This paper is organized as follows: section 2 provides a brief background on radiation force and details the methods used during ARFI imaging data acquisition. Section 3 describes the *in vitro* experimental setup and results from experiments. Section 4 provides results from the *in vivo* ovine model. Section 5 introduces three challenges associated with using ARFI for RF ablation guidance and presents results from experiments supporting the clinical feasibility of the technique. Section 6 includes a summary and discussion of the results presented and plans for future experiments.

2. Methods

2.1. Radiation force

Radiation force is a phenomenon associated with acoustic waves propagating through a dissipative medium. The body force (F, kg s^{-2} m^{-2}) created at the focus of an ultrasonic beam can be described by (Nyborg 1965, Torr 1984)

$$F(\vec{r},\ t) = \frac{2\alpha I(\vec{r},\ t)}{c}, \tag{1}$$

where α (m^{-1}) is the attenuation coefficient of the medium, I ($W\ m^{-2}$) is the local acoustic beam intensity and c ($m\ s^{-1}$) is the speed of sound in tissue. The magnitude of F is proportional to α, indicating a dependence on both the intrinsic material properties of the target media and the transmit frequency utilized. The applied force is in the direction of the energy density gradient, which in absorbing media (such as tissue) is in the direction of wave propagation.

In ARFI imaging, high-intensity, short-duration, focused acoustic beams are used to apply radiation forces to target regions of tissue. Tissue response to an applied radiation force is determined by several factors, including its viscoelastic properties and boundary conditions associated with surrounding media. In general, assuming a uniform distribution of radiation force, displacement magnitude is inversely related to local tissue stiffness. ARFI imaging utilizes conventional ultrasonic pulses to monitor the tissue response both spatially and temporally. A single transducer on a diagnostic ultrasound scanner is used to both generate radiation forces and track the ensuing tissue displacements. Further information concerning radiation force and ARFI imaging is provided by Nightingale *et al* (2002).

2.2. Data acquisition

B-mode and ARFI images were acquired with a Siemens SONOLINE Antares™ scanner (Siemens Medical Solutions USA Inc., Ultrasound Division, Issaquah, WA) that has been modified to provide users with the ability to specify acoustic beam sequences and intensities, as well as access raw radiofrequency echo data. A Siemens CH6-2 curvilinear transducer array operating at 2.5 MHz was used to acquire data. Transmit *F*/numbers were chosen to optimize the trade-off between lateral resolution and depth-of-field, and ranged from 2.5 to 3.5. Dynamic focusing and aperture growth were utilized in receive so that a constant *F*/number was maintained.

ARFI image beam sequences consisted of both pushing and tracking beams. Tracking beams were standard B-mode ultrasound pulses, while pushing beams were unapodized ultrasound beams with pulse lengths ranging from 160 to 320 μs. Image focal depths were selected to correspond to structures being imaged and ranged from 6.5 to 9 cm. Two-dimensional ARFI images were made by electronically translating the active transducer aperture through 30-72 pushing locations spaced radially by 0.6-1.7 mm at the beam focus. *In vivo* data acquisition was performed using ECG-triggered beam sequences, with data acquisition occurring in late diastole.

Parallel receive tracking was implemented during several *in vitro* and phantom experiments. This technique allows for up to four lines of the tissue dynamic response to be recorded simultaneously after each individual pushing beam is fired (Dahl *et al* 2005, in preparation). Thus, a conventional ARFI image requiring 72 pushing locations can be acquired using as few as 18 pushing locations if parallel receive displacement tracking is utilized, without accompanying sacrifices of field-of-view (FOV) or sampling density. In homogeneous media, displacements measured at each of the four off-axis receive locations are generally uniform if time is given to allow for shear waves to propagate to outer tracking regions. Although tracked displacements are uniform, each displacement will slightly underestimate the peak displacement that could be tracked along the pushing beam axis. This issue will be treated more extensively in the discussion section.

2.3. Image processing and visualization

Displacement data were processed off-line by performing 1D cross-correlation in the fast-time dimension between a reference tracking beam and sequentially acquired tracking beams transmitted after the application of radiation force (Trahey *et al* 1987, O'Donnell *et al* 1994). Each tracking line was divided into a series of search regions, and the location of the peak in

the cross-correlation function between a 0.92 mm kernel in the first tracking line and a search region in the next tracking line was used to estimate axial tissue displacement in that region. The kernel regions overlapped one another by 98%. Linear motion filters were applied to *in vivo* data in order to minimize artefacts stemming from transducer or physiological motion (Nightingale *et al* 2002).

ARFI displacement images acquired at a pre-determined time following the removal of radiation force were processed and displayed in real time on the monitor of the ultrasound scanner or on a separate display. Real-time ARFI implements the Kasai autocorrelation algorithm (Kasai *et al* 1985) using raw RF echo data acquired from the Antares scanner. The Kasai algorithm is generally associated with decreased performance relative to the normalized cross-correlation algorithm used in off-line processing, but can be implemented with nearly an order of magnitude decrease in computation time (Pinton *et al* at press). The data are ported to an eight-node Linux cluster with 3.2 GHz Pentium IV processors and 1 GB of RAM over 100 Mbit ethernet. The system calculates displacements down to 0.2 μm with a self-balancing master-slave algorithm written with the message passing interface. Communications between processors occur over a 1 Gbit ethernet network. Temporal linear motion filtering and two-dimensional spatial median filtering are included in the algorithm. The dynamic range of the output image is determined based upon the image histogram. The frame rate for real-time ARFI imaging is computationally limited to 12 Hz, though transducer heating and patient acoustic exposure restrict the achievable frame rate in most applications. Alternatively, a similar algorithm can be implemented at 0.5-1 Hz on a 1.7 GHz Pentium M laptop computer with 1 GB of RAM.

Selected images were further processed off-line using time-gain control (TGC) techniques. TGC algorithms apply an angularly independent, axially varying gain to raw displacement data in order to normalize for gradients in applied force in the focal region of the pushing beams. This technique generally results in improved image contrast and an expanded range of depths over which relative stiffness differences can be visualized. A detailed description of this algorithm has been provided previously (Fahey *et al* 2005a). TGC-processed images have a scale of relative displacement, as opposed to conventional ARFI images, which have a scale of absolute displacement. Throughout this paper, TGC-processed images will be shown in a different colour map than conventional ARFI images in an effort to avoid confusion of image scale.

3. *In vitro* experiments

3.1. Experimental setup and procedure

In vitro experiments were performed on freshly excised bovine livers purchased from a local butcher. Large subsections (approximately 30 cm × 15 cm × 10 cm) of the livers, chosen for their high degree of uniformity, were selected for use in the study. Sections of liver were placed in a deionized water bath and were degassed in a 650 mmHg vacuum chamber over a period of 4-6 h. Upon removal from the vacuum chamber, liver samples were promptly placed into a windowed water tank and anchored in place.

A Radionics Cool-Tip RF ablation system (Valleylab/Tyco Healthcare Group, Boulder, CO) was used to induce thermal lesions in the bovine liver samples. A three-prong ablation electrode cluster with 2.5 cm active tip exposures was inserted into the liver sample through the top of the water tank, as shown in figure 1. The imaging transducer was aligned perpendicular to the ablation electrode cluster. Reference B-mode and ARFI images were acquired prior to ablation in order to record initial tissue echogenicity and stiffness. A pre-programmed, impedance-controlled, 12 min ablation procedure was performed on the liver samples in accordance with the recommended settings from the device manufacturer. B-mode and ARFI images were

acquired during and after the RF ablation procedures were performed. Although much faster rates were available for use, image acquisition rates during the procedures ranged from 1 to 4 images min^{-1}, with the maximum rate of 4 images min^{-1} selected based upon experimental observations of the smallest perceptible changes in thermal lesion size in ARFI images. Following imaging, liver samples were removed from the water tank and sliced in the approximate imaging plane of the transducer in order to assess the induced thermal lesion. Photographs were taken to record thermal lesion size and shape.

3.2. Experimental results

Results from an *in vitro* liver ablation experiment are shown in figure 2. In this experiment, B-mode and ARFI images were acquired at a rate of 1 image min^{-1} over the course of the 12 min ablation procedure. The ARFI imaging beam sequence used for data acquisition consisted of 72 pushing locations separated radially by 0.55 mm at the beam focus (7 cm). Each pushing pulse in this experiment was 160 μs in duration. An *F*/number of 2.5 was used in transmit.

Figures 2(a) and (b) show reference B-mode and ARFI images, respectively, of the liver sample before the insertion of the ablation electrode cluster. The ARFI image in figure 2(b) has been centred in its B-mode companion image for anatomical reference. As expected, prior to ablation the liver sample is fairly uniform in both echogenicity and stiffness throughout the tissue region under investigation (depths of 1-7 cm).

Figures 2(c) and (d) show B-mode and ARFI images acquired 3 min into the ablation procedure. The location of the ablation electrode is easily seen in figure 2(c), as noisy reverberations from the electrode prongs are present in the image at depths beyond the insertion point (approximately 5 cm). These reverberations also create a region of artefact (blue region in centre) in the ARFI image. Displacement data in this region are static through the tracking interval (i.e. changes only due to noise, no displacement/recovery) and are nearly identical to data collected after the electrode was inserted but prior to commencement of ablation (not shown). Thus, the presence of the electrode cluster creates an effective stiffening artefact in the ARFI image, and with this transducer orientation, stiffness changes in this portion of the liver sample associated with thermal lesion development will be obscured by this image artefact.

Figure 2(e) shows the ARFI image acquired after 7 min of ablation. At this point, the lesion diameter has increased 5 mm in the lateral dimension and its boundaries extend 4 mm further into the near field relative to the image in figure 2(d). The edges of the growing thermal lesion have extended beyond the region of the image corrupted by artefacts and nearly all of the lesion boundaries can be distinguished well from the untreated liver tissue. The exception is the distal lesion boundary, which remains masked by the presence of the ablation electrode cluster in the liver sample. Figure 2(f) shows the ARFI image acquired immediately following the cessation of RF delivery to the tissue, while the electrode cluster was still in place. Qualitative comparisons of figure 2(f) to the final image in figure 2(h) indicate that almost all of the lesion boundaries are visible at this point in time. The distal lesion boundary, however, remains obscured by the prongs of the ablation electrode. This masking of the distal lesion boundary is due to the relative orientations of the transducer and electrode cluster and is a phenomenon that has been reported previously by other groups (Varghese *et al* 2003).

Figures 2(g) and (h) show B-mode and ARFI images acquired within 2 min after the completion of the RF ablation procedure, after the ablation electrode had been removed. There is little change in the B-mode image compared to the reference B-mode image shown in figure 2(a), but comparison of the post-ablation (figure 2(h)) and reference (figure 2(b)) ARFI images clearly shows the presence of the induced thermal lesion (blue elliptical region). In figure 2 (h), all lesion boundaries are clear, and lesion size, shape and location can be readily

determined. The noisy region in the centre of the lesion likely stems from gas bubbles or water from the tank occupying the puncture holes created by the ablation electrode prongs. Gas bubble formation often occurs in the centre of thermal lesions induced in *in vitro* tissues (Fahey *et al* 2004) and generally leads to local reductions in image quality. Further reflection on this issue will be included in the discussion section.

A well-documented phenomenon in ARFI imaging is a reduction in applied radiation force beyond the acoustic transmit focus of the image (see, for example, Fahey *et al* (2004,2005a), Nightingale *et al* (2003)). In the ARFI images shown in figure 2, this phenomenon accounts for the reduced displacements at depths beyond 7 cm. If the induced thermal lesion had been of greater size, the distal lesion boundary would have been located beyond 7 cm and therefore would have been difficult to see in figure 2(h), even after the removal of the ablation electrode. A solution is to implement TGC processing techniques (Fahey *et al* 2005a) to normalize for gradients in applied radiation force throughout the focal region of the pushing beams. The TGC-processed version of figure 2(h) is shown in figure 2(i). Here we see similar lesion size, shape and boundaries as in figure 2(h), but qualitative stiffness comparisons can now be made throughout the entire 7.5 cm field of view. The image in figure 2(i) has a scale of relative displacement (as opposed to figures 2(b), (d)-(f) and (h), which have scales of absolute displacement) and is shown in a different colour map to reflect this change.

Results from a second *in vitro* liver ablation experiment are shown in figure 3. The experimental setup was identical to the procedure documented in figure 2, only the image acquisition rate was increased to 4 images min^{-1} in order to better sample the thermal lesion's growth through time. In addition, a more efficient ARFI imaging beam sequence, consisting of 30 interrogation locations spaced radially by 1.8 mm at the beam focus (8 cm), was used. This beam sequence utilized a transmit *F*/number of 2.5 and a pushing pulse length of 320 μs.

Figures 3(a) and (b) show reference B-mode and ARFI images, respectively, taken before the insertion of the ablation electrode cluster. Similar to the results shown in figure 2, initially the liver sample is fairly uniform in both stiffness and echogenicity throughout the tissue region being examined. Figures 3(c) and (d) show the B-mode and ARFI images acquired 90 s after the 12 min RF ablation procedure, following the removal of the ablation electrode cluster. The increase in echogenicity (due to gas bubble formation during RF ablation) in portions of the post-ablation B-mode image relative to the reference image indicate that a morphological change has likely occurred, but lesion size, location and boundaries are not easily inferred from this increase in brightness. Conversely, comparison of the reference and post-ablation ARFI images clearly shows that the RF ablation created a region of stiffened tissue (blue region) in a previously softer section of liver. This zone of stiffened tissue, elliptical in cross section, corresponds to the zone of thermal necrosis associated with the induced thermal lesion.

Figure 3 shows only reference and post-ablation B-mode and ARFI images of the RF ablation procedure. However, the increased frame rate used while monitoring this procedure allowed for the radial thermal lesion growth to be monitored through time with adequate temporal resolution. A movie documenting radial lesion growth, as monitored by ARFI imaging, is available on the authors' website (http://ultrasound.bme.duke.edu/pmb/ablation/movies.html). In the movie, there are periods of time when lesion visualization is partially obscured due to the presence of gas bubbles at the ablation site, but the majority of the induced lesion and its boundaries are easily discerned at any given time.

The TGC-processed version of the image shown in figure 3(d) is shown in figure 3(e). The normalization curve used to create figure 3(e) is shown in figure 3(f). Original displacement magnitudes at each depth were divided by the appropriate value in figure 3(f) to apply an

angularly independent, axially varying gain to the original displacement data shown in figure 3(d). Both the thermal lesion and the surrounding untreated liver tissue are best visualized in figure 3(e).

Figure 4 shows a photograph of the lesion imaged in figure 3. During imaging, the transducer was positioned to the right of the liver sample as it is oriented in the photograph. Limitations imposed by the experimental setup prevented precise registration between the cross section of the thermal lesion shown in figure 4 and the imaging plane of figure 3. However, the elliptical shape of the lesion cross section is apparent in both the photograph and the image, although the long axis/short axis ratio is slightly greater in the image. This topic will receive greater attention later in this paper.

4. *In vitro* experiments

4.1. Animal preparation and ablation protocol

Two sheep were used in this study approved by the Institutional Animal Care and Use Committee at Duke University conforming to the Research Animal Use Guidelines of the American Heart Association. Anaesthesia was induced and maintained with isoflurane gas (1-5%). Intravenous (IV) access was obtained and the animal was placed on a water-heated thermal pad. A tracheostomy was performed and the animal was mechanically ventilated with 95-99% oxygen. To prevent rumenal typany, a nasogastric tube was passed into the stomach. Electrolyte and ventilator adjustments were made based on serial electrolyte and arterial blood gas measurements. An IV maintenance fluid with 0.9% sodium chloride was infused continuously. Blood pressure, lead II ECG and temperature were continuously monitored throughout the procedure.

In each experiment, two ablations were performed in the liver of the animal. The ablation algorithm utilized was identical to the automated algorithm described in the previous section. Three RF ablation procedures were performed with the ablation electrode inserted transcutaneously into the liver through the intercostal space. One RF ablation procedure was performed with the electrode inserted through the diaphragm into the liver under open-abdomen conditions. Following animal sacrifice, livers were removed and placed in a refrigerated saline bath for approximately 12 h before they were examined. Photographs were taken to record thermal lesion size and location. When feasible, thermal lesions were induced in the vicinity of anatomical landmarks that could be used to facilitate comparisons between images and photographs from pathology.

Reference B-mode and ARFI images were acquired prior to each RF ablation procedure to record initial tissue echogenic and mechanical properties. B-mode and ARFI images were acquired every 15-20 s during and immediately following RF ablation procedures. Additional images were acquired of ablation sites 60-90 min after completion of the RF ablation protocol, following the completion of unrelated experiments involving the same animal. Data acquisitions were ECG triggered and completed during an animal breath-hold in order to minimize image artefacts stemming from physiological motion. During transcutaneous ablation procedures, the transducer was placed in the intercostal space. When performing RF ablation through an open abdomen, the transducer was placed directly on the animal's diaphragm in order to better simulate the scanning depths that would be encountered during transcutaneous imaging. All images were acquired with a hand-held Siemens CH6-2 transducer oriented with the axial dimension angled 45-90° to the ablation electrode. B-mode and ARFI images were displayed in real time on the monitor of the ultrasound scanner, an adjacent laptop computer, or both.

4.2. Experimental results

Figure 5 shows results from an ablation performed through an open abdomen in an *in vivo* ovine liver. (a) and (b) show reference B-mode and ARFI images taken after the insertion of the ablation electrode. Images that were acquired approximately 70 min following the completion of the RF ablation procedure are shown in (c)-(e). To optimize image quality, it was desired to allow some time post-procedure for gas bubble resorption. Although our experience and relevant literature (Raman *et al* 2000) indicate that bubbles will be absorbed over much shorter time spans, logistical difficulties associated with unrelated research involving the same animal prevented earlier post-ablation images from being obtained. Figures 5(f) and (g) show photographs of the excised liver taken 12 h after the ablation procedure. The imaging planes in figures 5(d) and (e) closely match the photograph planes in figures 5(f) and (g), respectively.

The reference B-mode image is shown in figure 5(a). The relatively hypoechoic region that spans the image above the dotted line is the diaphragm. Hepatic tissue occupies the majority of the image below the dotted line. The bowel lumen is indicated by the black arrow and the animal's gallbladder is indicated by the white arrow. Although the ablation electrode is close to the tissue region shown in the image, the tip of the electrode is not actually in the imaging plane, as evidenced by the lack of noisy ringdown in figure 5(a) that was seen in figure 2(c).

The reference ARFI image is shown in figure 5(b). The beam sequence used to create the image consisted of forty-four 280 μs pushing beams spaced radially by 1.5 mm at the beam focus (6.5 cm). Most of the hepatic tissue in the image is initially fairly uniform in stiffness and is displaced 3.5-5 μm by the applied radiation force. There is a region of liver tissue (enclosed in dotted circle) that appears slightly stiffer than neighbouring liver tissue due to the presence of the ablation electrode nearby. The fatty layer of tissue between the liver and the bowel is displaced the most (5+ μm) by the radiation force. Negligible displacements are induced in the tissue surrounding the bowel and in the gallbladder.

Post-ablation B-mode and ARFI images having a similar imaging plane as the reference images are shown in figures 5(c) and (d). The elevation plane of the image has moved slightly so that the relative positions of the gallbladder and bowel have been shifted. The dotted line in figure 5(c) indicates the boundary between the fatty tissue below the liver and the tissue surrounding the bowel. The B-mode image shows subtle indications of the presence of an induced thermal lesion, as a hypoechoic region now appears in the centre of the image. However, the boundaries of the hypoechoic region are ambiguous, particularly in regions more proximal than 4 cm. The arrows in figure 5(c) indicate the apparent location of the distal lesion boundary.

The induced thermal lesion is visualized with increased contrast in the ARFI image shown in figure 5(d). The induced displacement magnitudes in the liver tissue at the edges of the image and in the fatty tissue (white arrow) between the liver and the bowel have not changed significantly relative to the reference ARFI image shown in figure 5(b). However, a large region of reduced (~1.5 μm) displacement corresponding to the induced thermal lesion is now present in the centre of the image. Figure 5(e) shows a post-ablation ARFI image with an imaging plane perpendicular to that shown in figure 5(d). In this image, the white arrow points to a cross section of the portal vein, while the black arrow indicates the same fatty region of tissue shown by the arrow in figure 5(d). (It should be noted that the image in figure 5(e) is a mirror image of the original data, where the data have been flipped to aid comparisons with the pathology photograph shown in figure 5(g).) Contrast between the thermal lesion and the background liver tissue remains strong in this cross section of tissue, and all lesion boundaries are visualized well.

The pathology photographs shown in figures 5(f) and (g) closely represent the imaging planes shown in figures 5(d) and (e), respectively. Comparing figures 5(d) and (f), we see a close match between the shape of the lesion as depicted in the ARFI and pathology images, as both show the lesion with a relatively vertical right-side boundary and a more curved left edge. Although the gallbladder and some fatty tissue were removed before the photo in figure 5(f) was taken, portions of the fatty tissue indicated by the white arrow in figure 5(d) are visible in figure 5(f) (black arrow). Maximum lesion diameter is approximately 2.5 cm in the ARFI image and 3 cm in the photograph. A possible cause for this discrepancy in size is the fact that the two tissue planes are not identical.

A second comparison between ARFI images and pathology can be made with figures 5(e) and (g). Although the tissue planes match less closely than in the previous example, qualitative comparisons of lesion shape and relative location are still feasible. As in figure 5(e), the photo in figure 5(g) shows the thermal lesion (white arrow) lying adjacent to a fatty region of tissue (broken arrow) and just proximal to the portal vein (black arrow). The overall shape of the lesion as shown in the ARFI image is also confirmed by the photo.

Figure 6 shows an example of the real-time implementation of ARFI monitoring of RF ablation procedures. The radiologist (one of the authors, RCN) has inserted the ablation electrode (white arrow) transcutaneously into the liver of a sheep (bottom-right of photo) lying on the operating table. In his left hand is the ultrasound transducer, which is aimed at the ablation site. To his left, the real-time B-mode display on the ultrasound scanner has been temporarily replaced with still B-mode and ARFI images of the target site. Whenever a data acquisition is performed, these still images are displayed in less than 1 s on the monitor. After a user-defined time period, the still images are removed from the screen and live B-mode imaging resumes.

5. Additional feasibility experiments

5.1. Lesion size assessment

Limitations imposed by the experimental setup prevented accurate comparisons between the sizes of induced thermal lesions in ARFI images relative to pathology. However, precise area and volume measurements can be made using a custom tissue-mimicking phantom (CIRS Corporation, Norfolk, VA) with an embedded inclusion of known size. A series of 16 kPa nearly spherical inclusions with ~1 cm radius were embedded in a 4 kPa uniform backgroundmaterial at an array of depths. The pouring process used to create the inclusions caused them to become slightly elongated in the depth dimension, resulting in ellipsoidal inclusions. An example B-mode image of an inclusion central plane is shown in figure 7. In order to obtain a high-resolution image with easily discernible inclusion boundaries, a Siemens VF10-5 linear array operating at 6.67 MHz was used during acquisition. Assuming that B-mode image boundaries are reflective of actual inclusion size, the diameter is shown to be 2.05 cm in the lateral dimension and 2.15 cm in the axial dimension.

To evaluate areas and volumes of inclusions in abdominal ARFI images, a similar inclusion centred at a depth of 5.5 cm was investigated. A linear translation stage was used to sweep a CH6-2 transducer through the elevation plane in 1 mm increments, with images acquired at each location. Each ARFI image set consisted of 42 pushing locations separated radially by 1.0 mm at the beam focus (6.5 cm). Resulting displacement data were upsampled by a factor of 2 in the elevation dimension and subsequently normalized. Figure 8(a) shows the ARFI image of the central axial-lateral plane with the full dynamic range of displacement data. Inspection of the lateral inclusion/background interfaces in this image was used (in a manner blinded to both the B-mode data and other ARFI image planes) to determine a threshold of 55% of maximum displacement to represent the inclusion boundary. ARFI images of the three orthogonal, central planes through the inclusion with this displacement threshold are shown in

figures 8(b)-(d). This choice of threshold overestimates the known inclusion diameter by 1 mm in the elevation dimension. The distal axial boundary in figures 8(b) and (c) is located precisely in its known location, although the proximal axial boundary appears to extend about 1 mm further into the near field than expected. This apparent elongation of the inclusion will receive greater attention in the discussion section.

The true inclusion cross-sectional area was calculated from the B-mode image in figure 7. The inclusion boundaries were hand-selected by an observer unaware of potential lesion asymmetry and blinded to the ARFI data shown in figure 8. Five selected regions were averaged, with image pixels contained in at least three selections considered to lie within the inclusion. This method yielded an inclusion cross-sectional area of 3.41 cm^2. The data in figures 8(b)-(d) were used to calculate the apparent inclusion area in the central ARFI image planes. Using the same threshold of 55% of maximum displacement, the errors relative to the known cross-sectional area were 1.5%, 3.9% and 1.3% for the images shown in figures 8(b)-(d), respectively. The inclusion is not believed to be elongated in the lateral-elevation plane (d), and thus the true cross-section shape in this plane was assumed to be a circle with a diameter of 2.05 cm, as measured from figure 7.

The degree of contrast between the inclusion and the background material allows for the inclusion volume to be rendered from the ARFI displacement data using the same threshold value of 55%. This rendered volume is shown in figure 8(e). It is assumed that although the elongation of the inclusion in the axial dimension changed its shape, its overall volume can still be well approximated by that of a sphere with a 1 cm radius. In this case, with this choice of threshold, the apparent inclusion volume in the ARFI data was 4.35 cm^3, and thus overestimates the true inclusion volume by 3.8%.

5.2. Thermal lesion contrast

Effective implementation of ARFI imaging for real-time RF ablation guidance faces several challenges. One such challenge is achieving adequate image contrast under clinically realistic conditions, where thermal lesions are induced inside of target carcinomas rather than in non-tumorous regions of hepatic tissue. More specifically, it is vital to distinguish the developing lesion from the tumour being treated, which may already have an elevated stiffness relative to surrounding hepatic tissue. Thermal lesions have recently been measured to be 9-10 times stiffer than healthy liver (Bharat *et al* 2005), while several types of hepatic carcinomas have been measured to be 2-5 times stiffer than healthy liver under small strains (Yeh *et al* 2002). It is thus theoretically feasible to maintain adequate thermal lesion contrast in ARFI images of clinically realistic ablation sites.

To evaluate the impact of a tumorous ablation site on thermal lesion contrast, a custom tissue-mimicking phantom (CIRS Corporation, Norfolk, VA) was used. The phantom background was a uniform material with an approximate elastic modulus of 4 kPa. Two concentric nearly spherical inclusions (can be assumed spherical for present discussion) were used to simulate a clinically realistic imaging environment for monitoring RF ablation procedures. The outer sphere (diameter of 3 cm) had an elastic modulus of approximately 16 kPa and was used to model the hepatic carcinoma. The inner sphere (diameter of 1.5 cm) had an elastic modulus of approximately 30 kPa and was used to simulate a stiffened thermal lesion developing within the target tumour. Based upon the study results cited in the previous paragraph, it is likely that the stiffness contrast of the two spheres in the phantom is similar to the lowest tumour/lesion stiffness contrast one would expect to encounter *in vivo*. Both spheres were centred at a depth of 3 cm.

Figure 9 shows B-mode and TGC-processed ARFI images of the concentric spherical inclusions in the phantom. The ARFI image was created using 70 interrogation locations spaced

radially by 0.8 mm at the beam focus (4 cm) and 320 μs pushing pulse durations. Both of the spherical inclusions are visualized with good contrast in the ARFI image (figure 9(b)), with the inner sphere being displaced about 40% less by the applied radiation force than the outer sphere. There is also adequate contrast between the phantom background and the outer sphere, as the background material is displaced about 50% more by the radiation force excitation. In addition, the diameters of the sphere cross sections shown in the ARFI image match well with those exhibited in the B-mode image.

5.3. Physiological motion artefacts

A second challenge associated with ARFI monitoring of RF ablation procedures is image artefacts associated with physiological motion of target organs. Organs such as the heart and liver undergo significant physiological motion (Kolen *et al* 2004, Fahey *et al* 2005a, 2005b), which can lead to degradations in image quality if acquisition times are not sufficiently brief. Parallel receive tracking during ARFI imaging decreases acquisition times by allowing fewer, more widely spaced pushing beams to interrogate tissues in a desired FOV, and thus may help to minimize motion artefacts in images. This technique also allows for less thermal energy to be deposited into target tissues, which in turn allows for increased frame rates.

When implementing parallel receive tracking techniques, there are several beam sequence configurations that are available for use. For instance, if the FOV is held constant it is possible to decrease the number of necessary pushing beams, and thus acquisition times, by 50% while increasing the original sampling density of the tissue's dynamic response by a factor of 2. Alternatively, only 25% of the original number of pushing beams are necessary if it is only desired to maintain the original sampling density. However, in contrast to conventional ARFI imaging, parallel receive ARFI imaging samples the response of target tissues at some distance (for example, 0.6-2.4 mm radially at a depth of 8 cm) away from the pushing site. Particularly at times immediately following the removal of radiation force, reduced displacements may be recorded at these remote sampling locations relative to the central sampling location used in conventional ARFI imaging. The trade-off between acquisition time and image quality must therefore be assessed to maximize the utility of parallel receive ARFI for monitoring abdominal RF ablation procedures.

Figure 10 shows ARFI images of a stiff inclusion with a ~1 cm radius embedded in a custom tissue-mimicking phantom. Each image was created with a different number of transmitted pushing beams. Figures 10(a) and (b) are conventional ARFI images, with pushing and tracking beams fired along the same line of flight, while figures 10(c) and (d) are parallel receive ARFI images, with the tissue response sampled off-axis from the pushing beam. Figure 10(a) has 30 transmit and receive locations separated radially by 1.2 mm at the beam focus (8 cm) and figure 10(b) has 32 transmit and receive locations separated radially by 1.8 mm at the beam focus. Figure 10(c) has 20 transmit and 80 receive locations spaced radially by 2.4 mm and 0.6 mm at the focus, respectively. Figure 10(d) has 10 transmit and 40 receive locations spaced radially by 4.8 mm and 1.2 mm at the focus, respectively. Each beam sequence had a pushing pulse duration of 320 μs and a transmit *F*/number of 2.5. All images were created utilizing TGC processing and subsequently normalized, and have a scale of relative displacement. For reference, an identical 2.25 cm × 2 cm box has been placed around the inclusion in each image.

Inspection of figures 10(a) and (b) indicates little change in inclusion contrast or boundary definition when the line density is decreased by 33% in conventional ARFI imaging. The contrast and boundary definition similarity persists in figure 10(c) after implementing parallel receive tracking, although the apparent inclusion size has slightly decreased compared to figures 10(a) and (b). The decrease in size, particularly along the lateral dimension, is more evident in figure 10(d). This decrease in inclusion size in images using parallel tracking is likely attributable to the fact that the displacements being tracked result from shear wave

propagation. Shear wave dynamics in regions near the boundary of a spherical inclusion are complicated in nature (Palmeri *et al* at press), and boundary definition may suffer as the sampling density of displacement tracking beams is decreased. There are other potential causes, although further discussion of these issues is beyond the scope of this paper. A more elaborate discussion of topics associated with parallel receive ARFI imaging is provided by Dahl *et al* (submitted).

6. Discussion

The images presented in this paper show the potential for ARFI imaging in guiding RF ablation procedures in clinically realistic conditions. Thermal lesions are typically visualized with excellent contrast in ARFI images of both *in vivo* and *in vitro* liver tissues, being displaced 3-5 times less by applied radiation forces than surrounding untreated tissues. In general, the displacement contrast of a spherical inclusion subjected to impulsive radiation force is a complicated function of time, with dependency on both inertial effects and shear wave propagation. This phenomenon has been treated extensively in prior investigations (Nightingale *et al* 2006, Palmeri *et al* at press).

In tissue-mimicking phantoms, area and volume measurements of stiff inclusions in ARFI images agree with known parameters with a maximum error of less than 4%. This error is primarily due to a slight elongation of the true proximal inclusion boundary that occurs with the use of abdominal beam sequences. A similar proximal elongation is observed when comparing figures 3 and 4. This elongation effect is potentially caused by boundary condition effects reducing displacements induced in the phantom background material located just proximal to the stiff inclusion or by the fact that the curvature of the inclusion is small relative to the size of the elevation beamwidth at this depth. Further investigation into this phenomenon is needed. As the remaining inclusion boundaries are more well defined, future work involving spatial compounding of inclusion images acquired from different scanning angles may lead to improved boundary definition.

Preliminary comparisons suggest that ARFI imaging will also describe the sizes of induced thermal lesions with reasonable accuracy. Although the pathology comparisons presented in this paper are useful as qualitative indicators, logistical constraints associated with the experimental setup prevented precise size or volume comparisons from being made. Detailed studies investigating the correlation between lesion size in ARFI images and actual lesion size are underway. The effect of reactive hyperaemia on the size of thermal lesions in ARFI images is also unclear at this point. Reactive hyperaemia is a phenomenon not generally associated with *in vitro* tissues (Thomsen 1991, Liu *et al* 2004), and additional *in vivo* experiments are necessary to determine its impact on the accuracy of ARFI imaging.

As demonstrated in figure 2, changes in thermal lesion size can be detected in real time during RF ablation procedures. Perceptible changes of lesion size in ARFI images occur on a time scale of about 15 s. Although much faster frame rates are technically achievable, frame rates during extensive real-time ARFI imaging sessions will ultimately be limited by safety concerns related to tissue heating. Target tissue temperatures are increased during ARFI imaging as a result of both the absorption of ultrasonic energy and the transfer of heat from the transducer face to surface tissues. The limitations imposed on ablation monitoring protocols by thermal safety concerns will be addressed in a future publication.

Although real-time ARFI monitoring of RF ablation is often very successful, excessive gas bubble formation at the ablation site during the procedure can dramatically degrade image quality. This is particularly true *in vivo*, as blood perfusion tends to cause gas bubbles to spread away from the ablation site into neighbouring regions of tissue. There are several effects that

contribute to the degradation of image quality. First, reflection and absorption at the tissue-bubble interface reduces the magnitude of radiation forces applied in more distal regions. Second, applied radiation forces can induce a streaming of bubbles that results in large and often out-of-plane scatterer displacements. These large and unpredictable movements tend to decorrelate echo signals used in displacement calculations. Nevertheless, *in vivo* the majority of gas bubbles created during RF ablation procedures are resorbed within the first 0.5 h (or less) following surgery, at which time high-quality ARFI images can likely be made. Thus, even when tissue conditions prevent quality real-time monitoring of RF ablation procedures with ARFI imaging, the success of the procedure can still be assessed much earlier with ARFI than with methods currently implemented clinically. This is particularly useful for electrode repositioning, which is often necessary to treat larger tumours. It should be noted that Varghese *et al* (2004) have previously shown that movement of gas bubbles has minimal impact on the quality of elastography images acquired of *in vitro* RF ablation sites. Differences in the impact of gas bubbles on images acquired via radiation force and compressional elastography methods likely stem from differences in the nature of applied forces to tissues and the time scale over which tissue motions in a region are recorded.

The presence of the ablation electrode in the imaging plane can also impact the ability for ARFI imaging to monitor RF ablation, particularly early in the procedure. Depending on the relative electrode/transducer orientations, the electrode's presence can lead to stiffening or shadowing artefacts in ARFI images. Particularly when a three-prong electrode cluster is used, the rigid prongs can restrict the motion of surrounding tissues, leading to local stiffening artefacts that can mask the visualization of early lesion development. This effect can vary in severity (for example, large in figure 2 and less noticeable in figure 5) depending on transducer orientation. Another artefactual effect related to the electrode cluster is shadowing in ARFI images at depths beyond the insertion site. This artefact is caused by noisy ringdown from the metal electrode prongs which prevents accurate tracking of tissue displacements. Shadowing artefacts in ARFI images can often be eliminated by altering the scan angle used to interrogate the ablation site.

One challenge in utilizing ARFI to monitor RF ablation procedures *in vivo* is the significant amount of physiologic motion associated with abdominal organs. Organs such as the liver are displaced significantly by respiration and experience non-negligible motions associated with the cardiac cycle. Previous work (Fahey *et al* 2005b) has shown that abdominal ARFI images collected using ECG-triggered data acquisitions in conjunction with patient breath-hold are often successful at minimizing motion artefacts. Given the short (generally 100-300 ms) acquisition times associated with conventional ARFI imaging and the relatively slow frame rates (~1 image/15 s) needed to monitor thermal lesion growth in real time, this acquisition protocol is likely feasible for use in the clinic. This is especially true in the many institutions where RF ablation is performed under general anaesthesia, in which case patient ventilation can be directed by the interventionalist. Additionally, the recent implementation of ARFI imaging with parallel receive tracking significantly decreases acquisition times, thus making it easier to complete data acquisition during periods of minimal physiologic motion. Kolen *et al* (2004) have previously evaluated cardiovascular motion in the liver for applications in elasticity imaging. Similar studies are underway to assess the limitations physiologic motion will impose on ARFI imaging, which has different acquisition protocols than elastography and generally requires individual regions of tissue to be stable for shorter periods of time.

Parallel receive ARFI imaging holds much potential for increasing the utility of ARFI for RF ablation guidance. In addition to allowing for shorter acquisition times, parallel receive tracking allows for less energy, and thus heat, to be deposited into target tissues. Although image quality at depths which are clinically realistic for abdominal scanning may suffer as tracking lines move further away from pushing locations, the apparent clinical utility of these sparse images persists. For instance, the beam sequence used to create figure 10(d) could be used to detect

any complications which may occur early in an RF ablation procedure, with a more energetic sequence used to assess the growth and progress of the developing lesion at later stages. Given the thermal safety limitations inherent to radiation force excitations (Palmeri and Nightingale 2004), this protocol would allow for more images to be acquired throughout the procedure relative to exclusively using a more energetic sequence. Additionally, further development may improve the quality of sparsely sampled parallel ARFI images, and thus obviate the need for a more aggressive beam sequence entirely.

In this study, thermal lesions were only induced in non-tumorous regions of liver tissue. Thus, in practice, thermal lesion contrast may be lower than as shown figures 2, 3 and 5. However, figure 9 suggests that in clinically realistic situations it may be possible to differentiate the developing thermal lesion from the target tumour. Also, based upon previous experimental results (Fahey *et al* 2005b), we believe that many types of primary and secondary liver carcinomas will be visualized well *in vivo* with ARFI imaging. Thus, RF ablation procedures targeting isoechoic tumours, which would currently require the procedure to performed with CT or CT-fluoroscopy electrode guidance, may potentially be performed under ARFI guidance. This would save time, reduce costs and minimize radiation exposure to both the patient and the interventionalist.

In summary, from a functional standpoint ARFI imaging seems to be a promising modality for monitoring RF ablation procedures in real time. ARFI imaging is implemented entirely on a modified diagnostic ultrasound scanner, and thus it is inexpensive, portable and feasible for use in all patient populations. Also, as ultrasound is currently used during many RF ablation procedures for electrode placement, monitoring thermal lesion growth with ARFI imaging will not add additional cost or complicate the procedure with additional equipment.

Acknowledgments

The authors wish to thank Dale Bergman for her aid in the animal study and Joshua Baker-Lepain for his technical assistance. We thank Siemens Medical Solutions, USA, Ultrasound Division for their system support. This work was supported by NIH grants 1R01-HL-075485-02, 1R01-EB-002132-04 and 1R01-CA-114093-01.

References

Anderson G, Brinkmann F, Soulen M, Alavi A, Zhuang H. FDG positron emission tomography in the surveillance of hepatic tumors treated with radiofrequency ablation. Clin. Nucl. Med 2003;28:192–7. [PubMed: 12592125]

Bharat S, Techavipoo U, Kiss M, Liu W, Varghese T. Monitoring stiffness changes in lesions after radiofrequency ablation at different temperatures and durations of ablation. Ultrasound Med. Biol 2005;31:415–22. [PubMed: 15749565]

Cha C, Lee F, Gurney J, Markhardt B, Warner T, Kelcz F, Mahvi D. CT versus sonography for monitoring radiofrequency ablation in a porcine liver. Am. J. Roentgenol 2000;175:705–11. [PubMed: 10954454]

Choi D, Lim H, Lee W, Kim SH, Kim Y, Kim SH, Lim J. Early assessment of the therapeutic response to radio frequency ablation for hepatocellular carcinoma utility of gray scale harmonic ultrasonography with a microbubble contrast agent. J. Ultrasound Med 2003;22:1163–72. [PubMed: 14620886]

Dahl JJ, Pinton GF, Palmeri ML, Trahey GE. A parallel tracking method for acoustic radiation force impulse imaging. IEEE Trans. Ultrason. Ferroelectr. Freq. Control. submitted

Dahl JJ, Pinton GF, Trahey GE. Parallel receive beamforming for real-time ARFI imaging. Ultrason. Imaging 2005;26:259–60.(abstract)

Dodd G, Frank M, Aribandi M, Chopra S, Chintapalli K. Radiofrequency thermal ablation: computer analysis of the size of the thermal injury created by overlapping ablations. Am. J. Roentgenol 2001;177:777–82. [PubMed: 11566672]

Dodd G, Soulen M, Kane R, Livraghi T, Lees W, Yamashita Y, Gillams A, Karahan O, Rhim H. Minimally invasive treatment of malignant hepatic tumors: at the threshold of a major breakthrough. Radiographics 2000;20:9–27. [PubMed: 10682768]

Donckier V, Van Laethem J, Goldman S, Van Gansbeke D, Feron P, Ickx B, Wikler D, Gelin M. [F - 18] fluorodeoxyglucose positron emission tomography as a tool for early recognition of incomplete tumor destruction after radiofrequency ablation for liver metastases. J. Surg. Oncol 2003;84:215–23. [PubMed: 14756432]

Fahey B, Nightingale K, McAleavey S, Palmeri M, Wolf P, Trahey G. Acoustic radiation force impulse imaging of myocardial radiofrequency ablation: initial *in vivo* results. IEEE Trans. Ultrason. Ferroelectr. Freq. Control 2005a;52:631–41. [PubMed: 16060512]

Fahey B, Nightingale K, Nelson R, Palmeri M, Trahey G. Acoustic radiation force impulse imaging of the abdomen: demonstration of feasibility and utility. Ultrasound Med. Biol 2005b;31:1185–98. [PubMed: 16176786]

Fahey B, Nightingale K, Stutz D, Trahey G. Acoustic radiation force impulse imaging of thermally- and chemically-induced lesions in soft tissues: preliminary *ex vivo* results. Ultrasound Med. Biol 2004;30:321–8. [PubMed: 15063514]

Garcea G, Lloyd T, Aylott C, Maddern G, Berry D. The emergent role of focal liver ablation techniques in the treatment of primary and secondary liver tumours. Eur. J. Cancer 2003;39:2150–64. [PubMed: 14522372]

Gertner M, Worthington A, Wilson B, Sherar M. Ultrasound imaging of thermal therapy in *in vitro* liver. Ultrasound Med. Biol 1998;24:1023–32. [PubMed: 9809636]

Kasai C, Koroku N, Koyano A, Omoto R. Real-time two-dimensional blood flow imaging using an autocorrelation technique. IEEE Trans. Ultrason. Ferroelectr. Freq. Control 1985;32:458–63.

Kelekis A, Terraz S, Roggan A, Terrier F, Majno P, Mentha G, Roth A, Becker C. Percutaneous treatment of liver tumors with an adapted probe for cooled-tip, impedance-controlled radiofrequency ablation under open-magnet MR guidance: initial results. Eur. Radiol 2003;13:1100–5. [PubMed: 12695834]

Kolen A, Miller N, Ahmed E, Bamber J. Characterization of cardiovascular liver motion for the eventual application of elasticity imaging to the liver *in vivo*. Phys. Med. Biol 2004;49:4187–206. [PubMed: 15509060]

Krouskop T, Wheeler T, Kallel F, Garra B, Hall T. Elastic moduli of breast and prostate tissues under compression. Ultrason. Imaging 1998;20:260–74. [PubMed: 10197347]

Kruskal J, Oliver B, Huertas J, Goldberg S. Dynamic intrahepatic flow and cellular alterations during radiofrequency ablation of liver tissue in mice. J. Vasc. Interv. Radiol 2001;12:1193–201. [PubMed: 11585886]

Leyendecker J, et al. Sonographically observed echogenic response during intraoperative radiofrequency ablation of cirrhotic livers. Am. J. Roentgenol 2002;178:1147–51. [PubMed: 11959720]

Liu W, Techavipoo U, Varghese T, Zagzebski J, Chen Q, Lee F. Elastographic versus x-ray CT imaging of radio frequency ablation coagulations: an *in vitro* study. Med. Phys 2004;31:1322–32. [PubMed: 15259635]

Livraghi T, Goldberg S, Lazzaroni S, Meloni F, Ierace T, Solbiati L, Gazelle G. Hepatocellular carcinoma: radio-frequency ablation of medium and large lesions. Radiology 2000;214:761–8. [PubMed: 10715043]

Livraghi T, Goldberg S, Solbiati L, Meloni F, Ierace T, Gazelle G. Percutaneous radio-frequency ablation of liver metastases from breast cancer: initial experience in 24 patients. Radiology 2001;220:145–9. [PubMed: 11425987]

Lorentzen T, Christensen NE, Nolsle CP, Torp-Pedersen ST. Radiofrequency tissue ablation with a cooled needle *in vitro*: ultrasonography, dose response, and lesion temperature. Acad. Radiol 1997;4:292–7. [PubMed: 9110027]

Malcolm A, Ter Haar G. Ablation of tissue volumes using high intensity focused ultrasound. Ultrasound Med. Biol 1996;22:659–69. [PubMed: 8865561]

Mayo-Smith W, Dupuy D, Parikh P, Pezzullo J, Cronan J. Imaging-guided percutaneous radiofrequency ablation of solid renal masses: techniques and outcomes of 38 treatment sessions in 32 consecutive patients. AJR Am. J. Roentgenol 2003;180:1503–8. [PubMed: 12760909]

Montgomery R, Rahal A, Dodd G III, Leyendecker J, Hubbard L. Radiofrequency ablation of hepatic tumors: variability of lesion size using a single ablation device. AJR Am. J. Roentgenol 2004;182:657–61. [PubMed: 14975966]

Nightingale K, Palmeri M, Bouchard R, Trahey G. Proc. 2003 IEEE Ultrasonics Symposium. 2003

Nightingale K, Palmeri M, Trahey G. Analysis of contrast in images generated with transient acoustic radiation force. Ultrasound Med. Biol 2006;32:61–72. [PubMed: 16364798]

Nightingale K, Soo M, Nightingale R, Trahey G. Acoustic radiation force impulse imaging: *in vivo* demonstration of clinical feasibility. Ultrasound Med. Biol 2002;28:227–35. [PubMed: 11937286]

Nyborg, W. Physical Acoustics. Mason, W., editor. II B. Academic; New York: 1965. p. 265-331.chapter 11

O'Donnell M, Skovoroda A, Shapo B, Emelianov S. Internal displacement and strain imaging using ultrasonic speckle tracking. IEEE Trans. Ultrason. Ferroelectr. Freq. Control 1994;41:314–25.

Oudkerk M, Torres C, Song B, Knig M, Grimm J, Fernandez-Cuadrado J, Op de Beeck B, Marquardt M, van Dijk P, de Groot J. Characterization of liver lesions with mangafodipir trisodium-enhanced MR imaging: multicenter study comparing MR and dual-phase spiral CT. Radiology 2002;223:517–24. [PubMed: 11997562]

Palmeri M, McAleavey S, Fong K, Trahey G, Nightingale K. Dynamic mechanical response of spherical inclusions to impulse acoustic radiation force excitation. IEEE Trans. Ultrason. Ferroelectr. Freq. Control. at press

Palmeri M, Nightingale K. On the thermal effects associated with radiation force imaging of soft tissue. IEEE Trans. Ultrason. Ferroelectr. Freq. Control 2004;51:551–65. [PubMed: 15217233]

Pinton G, Dahl J, Trahey G. Rapid tracking of small displacements with ultrasound. IEEE Trans. Ultrason. Ferroelectr. Freq. Control 2006;53:1103–17. [PubMed: 16846143]

Raman S, Lu D, Vodopich D, Sayre J, Lassman C. Creation of radiofrequency lesions in a porcine model: correlation with sonography, CT, and histopathology. Am. J. Roentgenol 2000;175:1253–8. [PubMed: 11044017]

Righetti R, Kallel F, Stafford R, Price RE, Krouskop TA, Hazle JD, Ophir J. Elastographic characterization of hifu-induced lesions in canine livers. Ultrasound Med. Biol 1999;25:1099–113. [PubMed: 10574342]

Sharma A, Soo M, Trahey G, Nightingale K. Proc. 2004 IEEE Ultrasonics Symposium. 2004

Solbiati L, Goldberg S, Ierace T, Dellanoce M, Livraghi T, Gazelle G. Radio-frequency ablation of hepatic metastases: postprocedural assessment with a US microbubble contrast agent—early experience. Radiology 1999;211:643–9. [PubMed: 10352586]

Solbiati L, Ierace T, Tonolini M, Cova L. Guidance and monitoring of radiofrequency liver tumor ablation with contrast-enhanced ultrasound. Eur. J. Radiol 2004;51(Suppl):19–23. [PubMed: 15186880]

Thomsen S. Pathologic analysis of photothermal and photomechanical effects of laser-tissue interactions. Photochem. Photobiol 1991;53:825–35. [PubMed: 1886941]

Torr G. The acoustic radiation force. Am.J.Phys 1984;52:402–8.

Trahey G, Allison J, VonRamm O. Angle independent ultrasonic detection of blood flow. IEEE Trans. Biomed. Eng 1987;34:965–7. [PubMed: 2961682]

Varghese T, Shi H. Elastographic imaging of thermal lesions in liver *in vivo* using diaphragmatic stimuli. Ultrason. Imaging 2004;26:18–28. [PubMed: 15134391]

Varghese T, Techavipoo U, Liu W, Zagzebski J, Chen Q, Frank G, Lee F. Elastographic measurement of the area and volume of thermal lesions resulting from radiofrequency ablation: pathologic correlation. Am. J. Roentgenol 2003;181:701–7. [PubMed: 12933463]

Varghese T, Techavipoo U, Zagzebski J, Lee F. Impact of gas bubbles generated during interstitial ablation on elastographic depiction of *in vitro* thermal lesions. J. Ultrasound. Med 2004;23:535–44. [PubMed: 15098873]

Varghese T, Zagzebski J, Lee F Jr. Elastographic imaging of thermal lesions in the liver *in vivo* following radiofrequency ablation: preliminary results. Ultrasound Med. Biol 2002;28:1467–73. [PubMed: 12498942]

Xu H, Yin X, Lu M, Xie X, Xu Z, Liu G. Usefulness of three-dimensional sonography in procedures of ablation for liver cancers: initial experience. J. Ultrasound. Med 2003;22:1239–47. [PubMed: 14620896]

Yeh W, Li P, Jeng Y, Hsu H, Kuo P, Li M, Yang P, Lee P. Elastic modulus measurements of human liver and correlation with pathology. Ultrasound. Med. Biol 2002;28:467–74. [PubMed: 12049960]

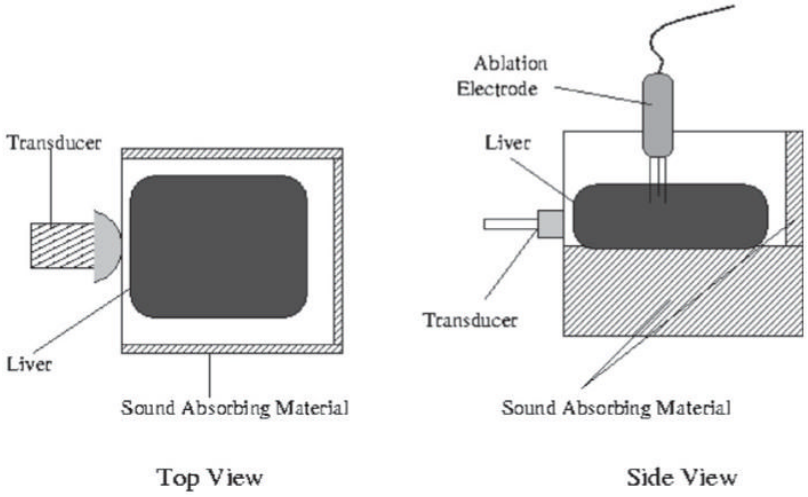

Figure 1.
Experimental water tank setup for ARFI monitoring of *in vitro* RF ablation.

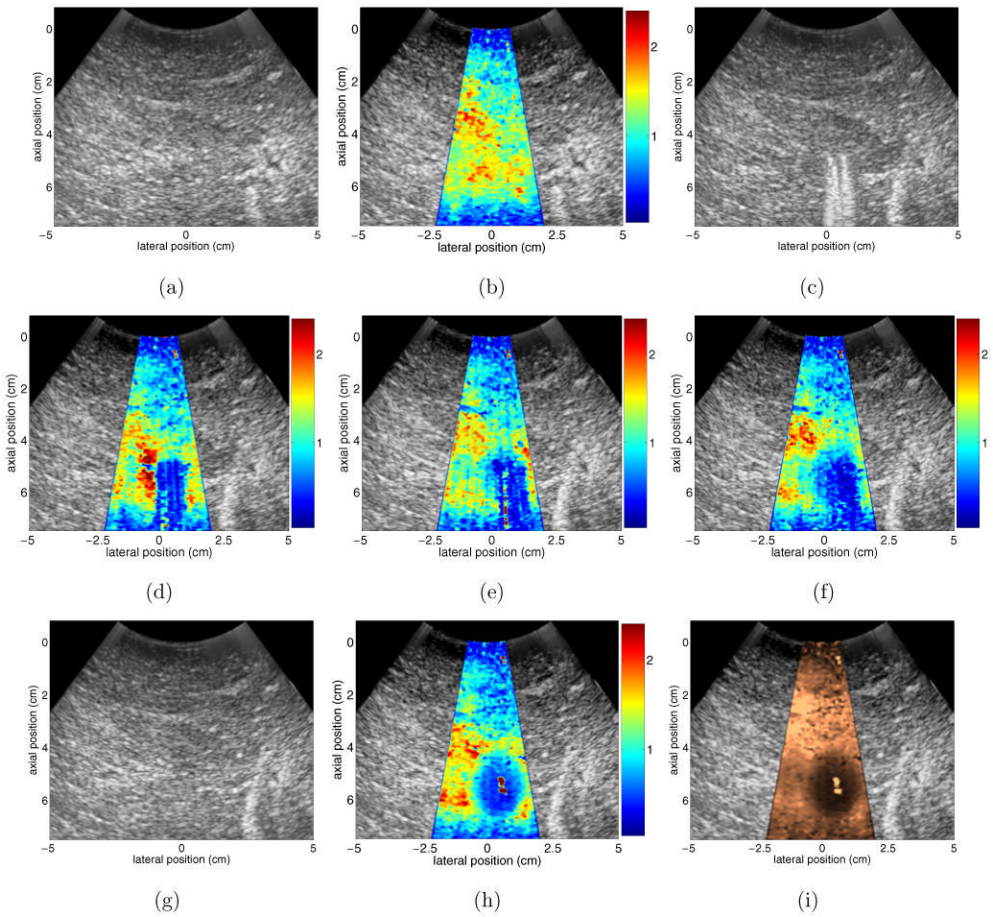

Figure 2.

Results from an *in vitro* RF ablation experiment performed on a freshly excised bovine liver sample. (a) and (b) show pre-ablation B-mode and ARFI images, respectively, that were acquired to record initial tissue properties. (c) and (d) show B-mode and ARFI images acquired 3 min into the RF ablation procedure. The presence of the ablation electrode cluster in the imaging plane creates artefacts in both (c) and (d). (e) and (f) show ARFI images acquired 7 and 12 min into the ablation procedure, respectively. (g) and (h) show B-mode and ARFI images acquired 2 min after the completion of the RF ablation procedure, after the electrode cluster has been removed from the sample. (i) is the image shown in (h) after the application of TGC processing. Scale of all ARFI images except for (i) is displacement in micrometres. (i) has a scale of relative displacement.

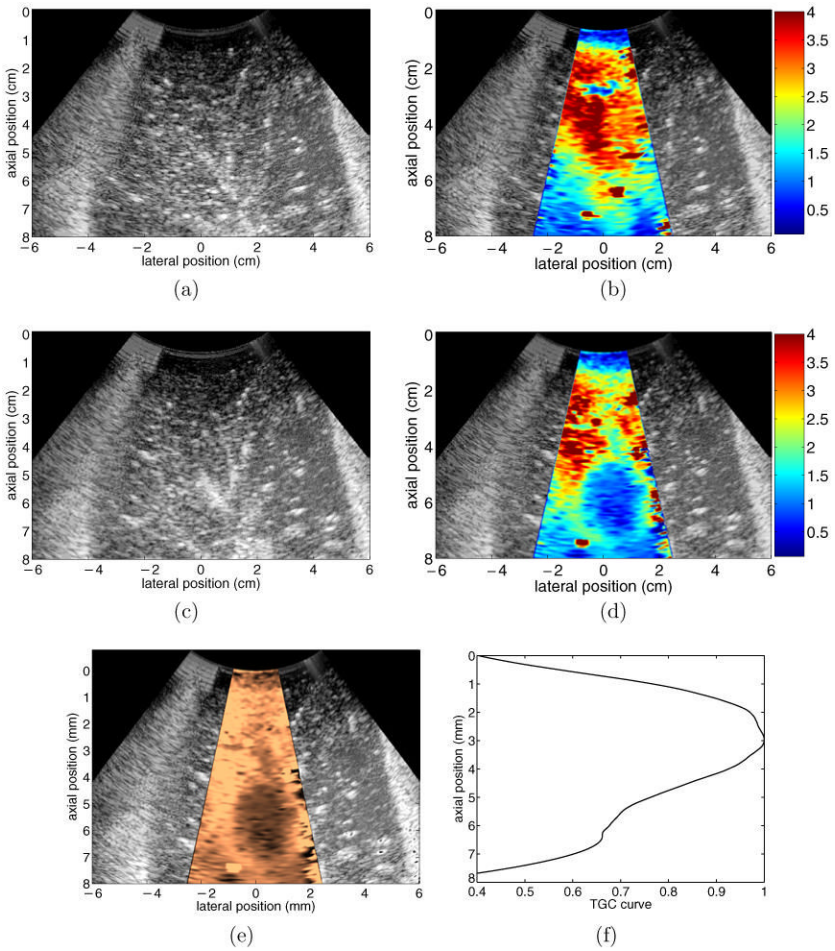

Figure 3.

Results from an *in vitro* RF ablation experiment performed on a freshly excised bovine liver sample. (a) and (b) show pre-ablation B-mode and ARFI images, respectively. (c) and (d) show B-mode and ARFI images acquired 90 s after the completion of the 12 min ablation procedure, after the ablation electrode cluster had been removed. (e) shows the data in (d) after the application of TGC processing. (f) shows the displacement-depth curve used to determine the appropriate axial gains applied to (d) to create (e). Scale of (b) and (d) is displacement in micrometres.

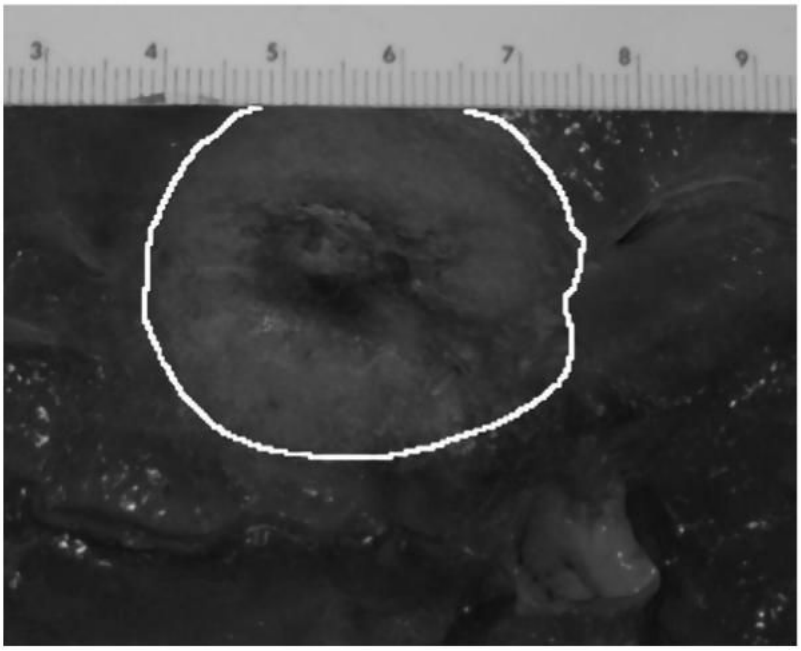

Figure 4.
Photograph of thermal lesion depicted in figure 3. During imaging the transducer was positioned on the right-hand side of the sample. Scale of ruler is cm.

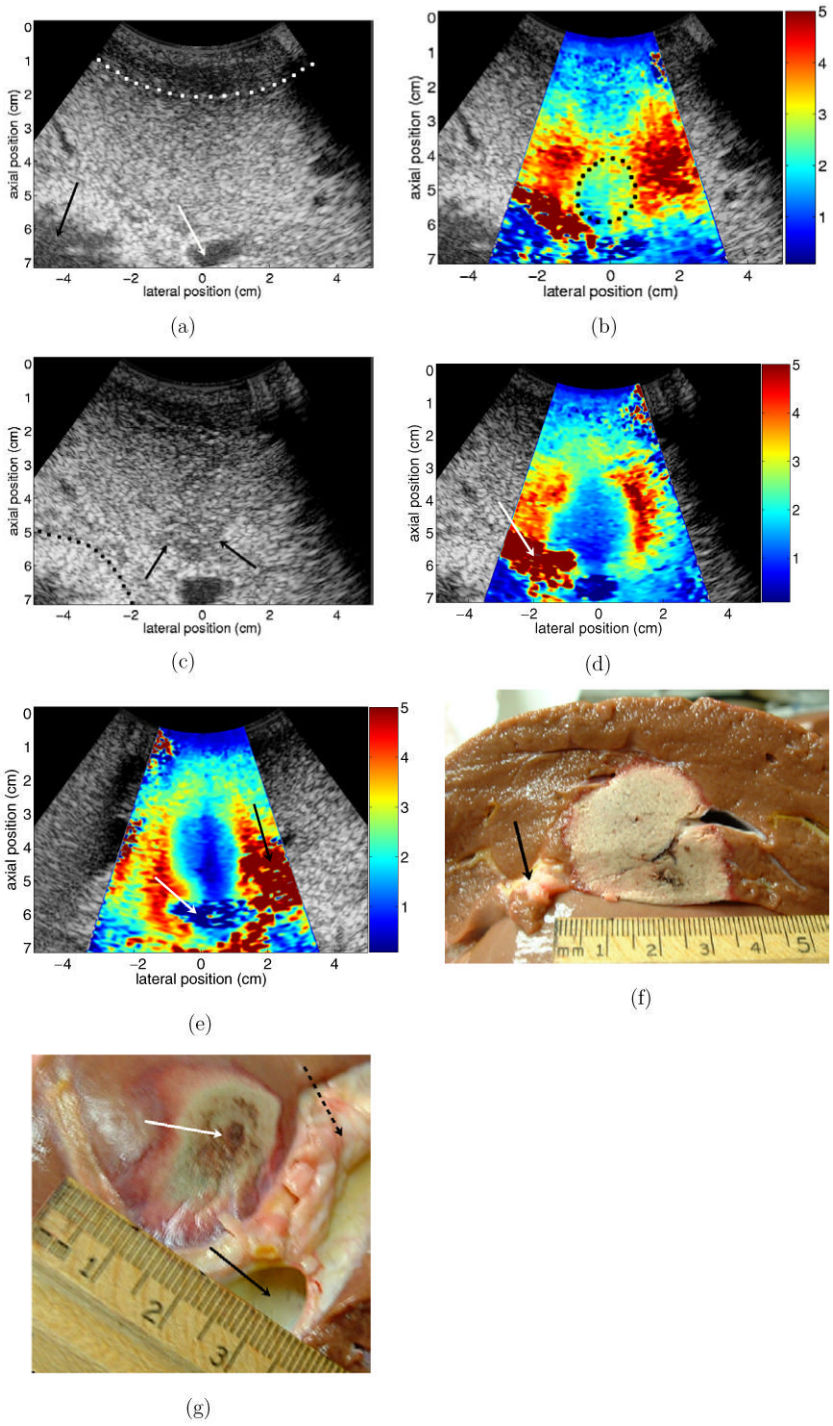

Figure 5.

B-mode, ARFI and pathology images from ablation of *in vivo* ovine liver. (a) and (b) show reference B-mode and ARFI images. (c) and (d) show B-mode and ARFI images acquired 70 min after ablation with the electrode still in place. (e) shows ARFI image with a perpendicular imaging plane to (d), after electrode has been removed. (f) and (g) show pathology images that closely match the imaging planes shown in (d) and (e). Black arrow in (a) indicates the bowel lumen, white arrow in (a) refers to the animal's gallbladder, dotted line in (a) indicates boundary

between diaphragm and liver. Dotted circle in (b) encloses region that is effectively stiffened by the presence of the ablation electrode. Dotted line in (c) indicates the boundary between fatty tissue and the tissue surrounding the bowel wall, arrows in (c) show the apparent distal boundary of the thermal lesion. Arrow in (d) points to pad of fatty tissue separating liver tissue from bowel. White arrow in (e) points to a cross section of the portal vein, black arrow in (e) points to fatty tissue region. Arrow in (f) indicates a section of fatty tissue shown in (d). Black solid arrow in (g) indicates the portal vein, broken black arrow in (g) indicates fatty tissue around the vessel and white arrow in (g) points to the centre of the induced thermal lesion.

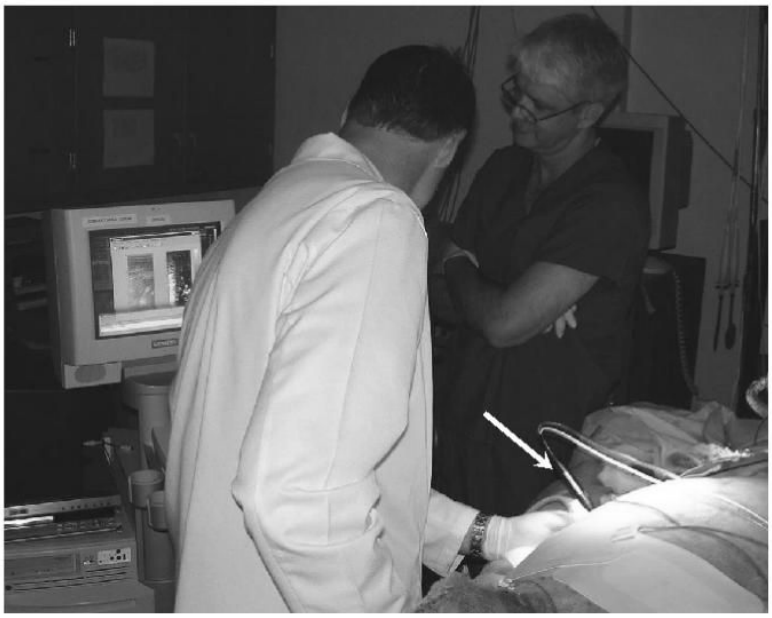

Figure 6.
Example of real-time implementation of ARFI monitoring of RF ablation *in vivo*. B-mode and ARFI images are acquired and displayed in real time on the monitor of the ultrasound scanner. White arrow points to the ablation electrode after its insertion into the animal's liver.

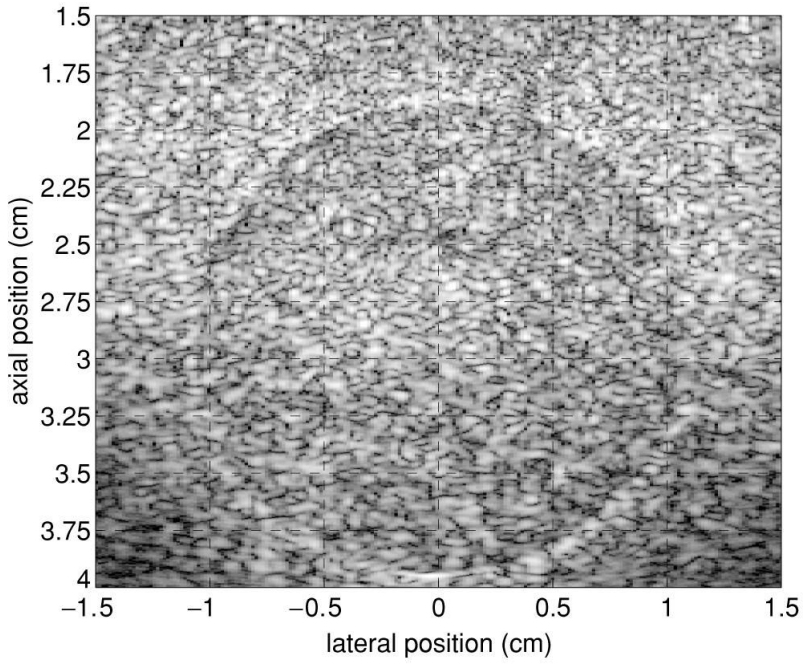

Figure 7.
B-mode image of a ellipsoidal inclusion embedded in a uniform tissue-mimicking phantom. Image acquired using a transmit centre frequency of a 6.67 MHz.

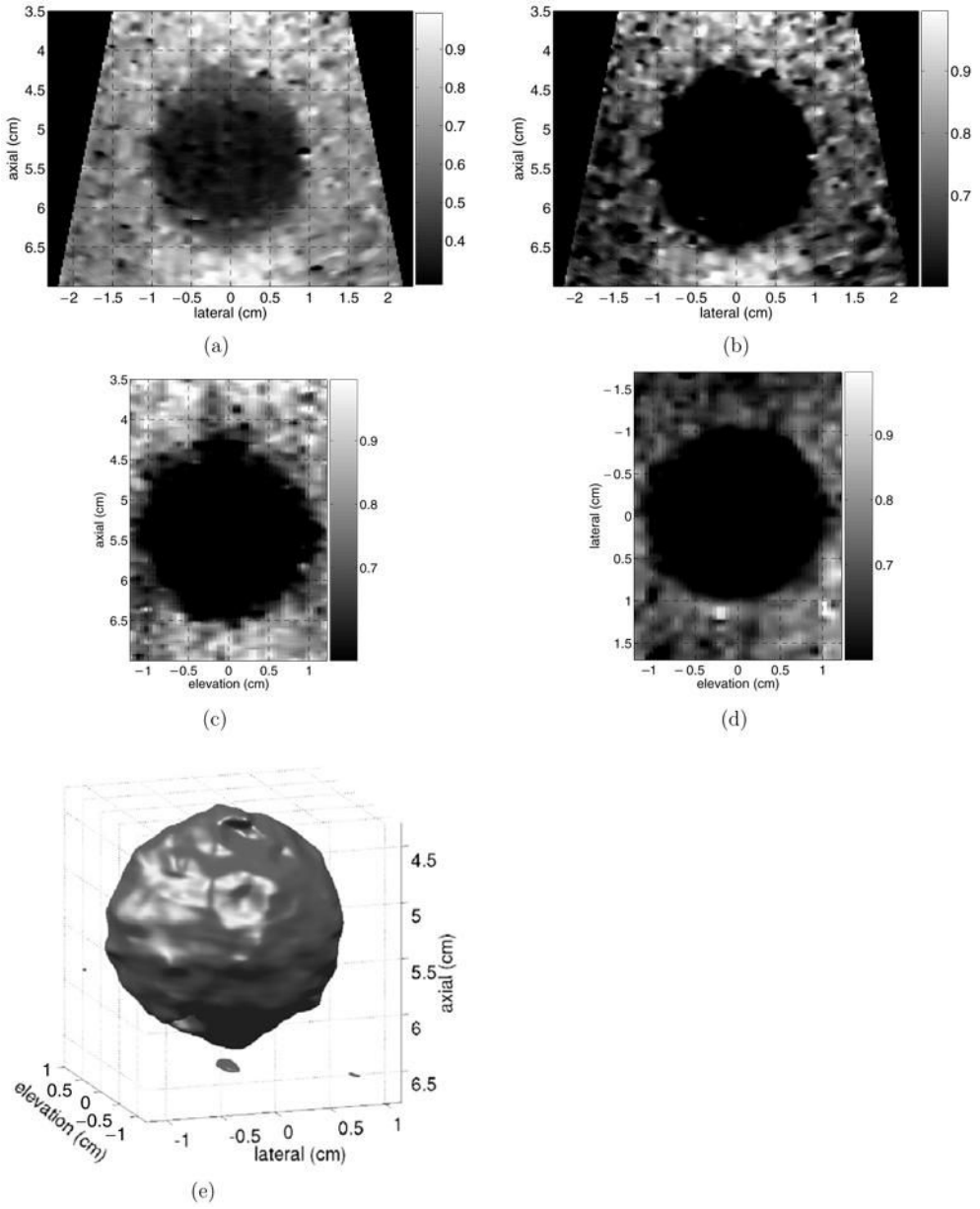

Figure 8.

Normalized ARFI images of three-dimensional volume of a ~1 cm radius stiff inclusion embedded in a tissue-mimicking phantom. (a) shows axial-lateral plane with full dynamic range. (b)-(d) show three orthogonal, central planes with a lower bound of 55% of maximum displacement applied. (e) shows 3D volume of stiff inclusion, rendered using a 55% threshold.

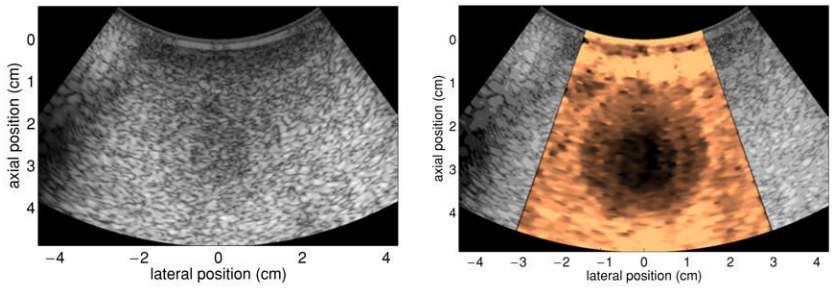

Figure 9.

B-mode (a) and TGC-processed ARFI (b) images of a tissue-mimicking phantom with concentric spherical inclusions. Outer sphere has a diameter of 3 cm and an elastic modulus of 16 kPa. Inner sphere has a diameter of 1.5 cm and an elastic modulus of 30 kPa. Phantom background material has an elastic modulus of 4 kPa. The TGC-processed ARFI image has a scale of relative displacement.

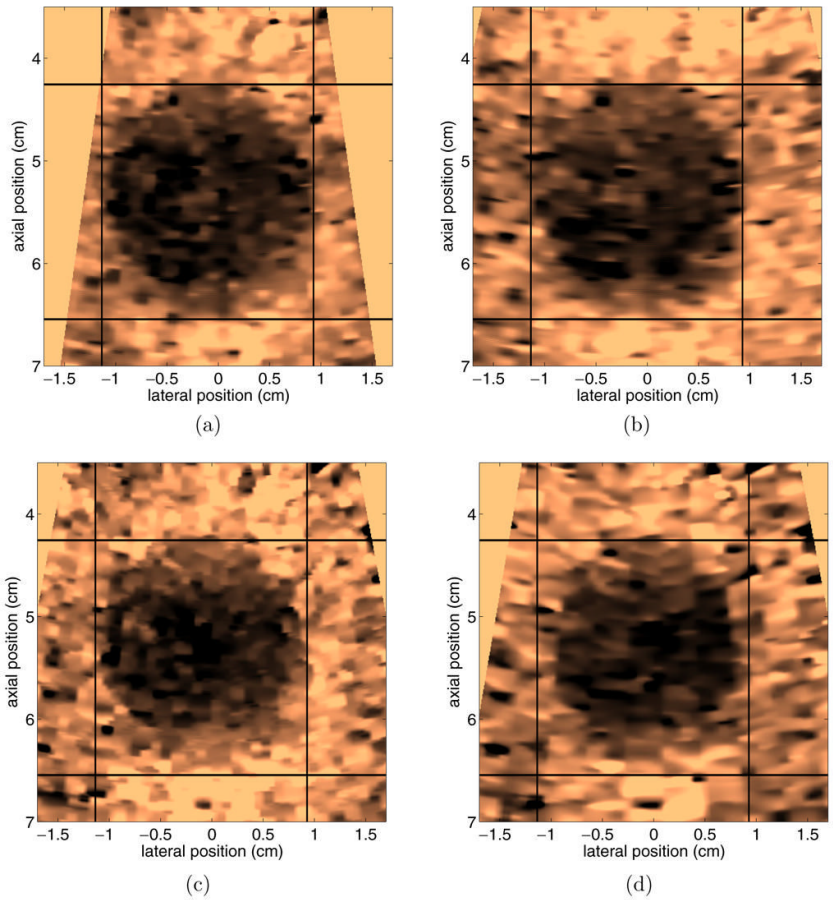

Figure 10.

Comparison of ARFI images acquired with different line densities. (a) has 30 transmit and receive locations separated radially by 1.2 mm at the beam focus, (b) has 30 transmit and receive locations separated radially by 1.8 mm at the beam focus. (c) and (d) use parallel receive so that four image lines are acquired per every transmit pushing location. (c) has 20 transmit and 80 receive locations spaced radially by 2.4 mm and 0.6 mm at the focus, respectively. (d) has 10 transmit and 40 receive locations spaced radially by 4.8 mm and 1.2 mm at the focus, respectively. All images were created utilizing TGC processing and normalized, and have a scale of relative displacement.